Multifrequency Backscattering Tomography for Constant and Vertically Varying Backgrounds

Ru-Shan Wu,* Fernanda Vieira Araújo, and Lian–Jie Huang[†]

PPPG/UFBA, Universidade Federal da Bahia, Salvador, BA 40210, Brazil

ABSTRACT

To improve the resolution and image quality of the SFDT (Single-Frequency Diffraction Tomography), a special fast multi-frequency imaging method: Multi-Frequency Backscattering Tomography (MFBT) is introduced in this paper. The method uses only the backscattered waves (after plane wave decomposition) while maintaining the merit of multi-frequency method. The method is formulated for both the constant and vertically varying backgrounds. For the latter case the WKBJ approximation is used for the background Green's function. Formulas are derived both for volume scattering using the Born approximation and for boundary scattering using the physical optics approximation. Two reconstruction methods are presented. The backpropagation method can be used and has the same computation speed for both the constant and vertically varying backgrounds. Meanwhile the direct FT method is only formulated for the constant background, in which the backpropagation in z-direction is implemented by FFT and therefore the computation speed is significantly increased. Compared with the SFDT using backpropagation reconstruction, the MFBT is nearly $N_z/log_2 N_z$ faster, where N_z is the number of grid points in z-direction, and at the same time has a much better resolution and image quality. When N_z is big, the time saving is remarkable. Compared with other multi-frequency methods such as the multi-frequency holography (prestack migration), the speeding factor becomes $N_f N_z/log_2 N_z$, where N_f is the number of frequencies used. Numerical simulations for both constant and vertically varying backgrounds are performed to demonstrate the feasibility of the method and the quality of reconstructed images for different situations. Examples are also given to show that when the reconstruction procedure of constant background is applied to the case of vertically varying background, the image quality will be greatly deteriorated. © 1994 John Wiley & Sons, Inc.

I. INTRODUCTION

Since diffraction tomography was introduced to geophysical applications [1, 2], it has been tested by numerical experiments and ultrasonic laboratory experiments [3, 4] and applied to different geophysical problems, such as fracture detection [5], salt pod imaging [6], buried waste detection [7], and dinosaur bone location [8]. However, diffraction tomography was formulated for the case of a monochromatic wave field and therefore has inherent problems, such as limited resolution and image distortion due to the existence of "blind areas" in the object spectrum. Since the sources used in seismic exploration or other applications (such as georadar subsurface imaging) are often broad banded, further development of geophysical diffraction tomography awaits the use of multifrequency (MF) approaches, which can improve the resolution and partly fill the blind areas of the object spectrum. Multifrequency holography [9, 2], which is similar to the process of prestack migration [10], has been shown to have improved resolution, especially vertical resolution, and image quality. For the geometry of nondestructive testing of materials, in which the plane-wave source is used to illuminate the object from all directions (full view), MF diffraction tomography has been used in a straightforward way [11]. However, in the case of geophysical applications, multi-frequency diffraction tomography has rarely been discussed in the literature.

In this paper, following the proposal of Wu [12], we formulate a special multifrequency linear inversion method, multifrequency backscattering tomography (MFBT), which has a fast computation speed and also offers improved resolution and image quality compared with single-frequency diffraction tomography (SFDT). First, we treat the case of uniform background in Section II and derive both the formulas for volume scattering using the Born approximation and the formulas for boundary scattering using the physical optics approximation. The latter is applicable for the case of a large homogeneous volume scatterer or strong interface reflection and scattering. It is shown that under certain approximations the boundary scattering problem ends up with the same formulas except for a factor which modifies the object spectrum. Then in Sec. III we present two reconstruction methods; the backpropagation method and the direct Fourier-transform (FT) method. In the latter method, the backpropagation of plane waves in the z direction is implemented by fast Fourier transform (FFT) through a change of variable and an interpolation of data along the frequency axis, and thus increases significantly the computation speed. In Sec. IV we extend the formulation to the case of vertically varying background using the WKBJ approximation for the background Green's function. The backpropagation method of reconstruction can be easily modified for this case. Finally, in Sec. V numerical examples are given to test the theory and methods.

Although the formulation and numerical examples in this paper are given for the 2D case, the theory and method can

---

* On leave from Institute of Geophysics, Chinese Academy of Sciences, Beijing, China. Present address: Institute of Tectonics, University of California, Santa Cruz, CA 95064.

† On leave from Institute of Geophysics, Chinese Academy of Sciences, Beijing, China. Present address: Institut du Physique du Globe de Paris, Paris 75252, France.

be generated to the 3D case in a straightforward way. There-fore the method presented in this work offers a feasible fast algorithm of imaging the subsurface 3D heterogeneities by wave tomography using 2D seismic array data. The method is also useful for the image reconstruction of georadar using electromagnetic waves.

II. CASE OF UNIFORM BACKGROUND

Here we consider only the 2D case. The generalization to the 3D case is straightforward. We start from the scalar wave equation

$$\left[\nabla^2 + \frac{\omega^2}{c^2(\mathbf{r})}\right]u(\mathbf{r}, \omega) = 0 , \tag{1}$$

where ∇^2 is the Laplacian operator, ω is the angular fre-quency, $c(\mathbf{r})$ is the wave propagation speed, which is a func-tion of the position $\mathbf{r}$, u is the wave field, which can be the pressure field in the case of acoustic waves or a component of the electric field in the case of electromagnetic waves. Define the object function $O(\mathbf{r})$ as

$$O(\mathbf{r}) = 1 - \frac{c_0^2}{c^2(\mathbf{r})} , \tag{2}$$

where c_0 is the wave speed in the background medium, and decompose the total field $u(\mathbf{r})$ into

$$u(\mathbf{r}) = u_0(\mathbf{r}) + U(\mathbf{r}) , \tag{3}$$

where $u_0(\mathbf{r})$ is the primary (or incident) field and $U(\mathbf{r})$ the scattered field. We can then have a formal solution of the scattered field from Eq. (1). In the case of SRP (surface reflection profiling) geometry, we have

$$U(x_g, x_s) = -\int_V k^2 O(\mathbf{r})u(\mathbf{r})G(x_g, \mathbf{r})\, \mathrm{d}V , \tag{4}$$

where $U(x_g, x_s)$ is the scattered field received by the geophone at x_g excited by a point source at x_s, $k = \omega/c_0$, $G()$ is the Green's function in the background medium. Equation (4) is an integral equation, since the total field contains the unknown scattered field. In order to linearize the inverse problem, we adopt two kinds of approximations. One is the Born approximation for weak scattering, the other is the PO approximation (physical optics approximation or Kirchhoff approximation) for large homogeneous bodies or smooth interfaces (boundary scattering).

A. Volume Scattering. In the case of weak volume scatter-ing for a point source with unit strength, apply the Born approximation $u(\mathbf{r}) \approx u_0(\mathbf{r}) = G(\mathbf{r}, x_s)$ to (4), and then double-Fourier-transform the equation along both the source line x_s and receiver line x_g, resulting in

$$\tilde{U}(k_g, k_s) = -\int_V k^2 O(\mathbf{r})\tilde{G}(k_g, \mathbf{r})\tilde{G}(\mathbf{r}, k_s)\, dV . \tag{5}$$

Substituting the Green's function of homogeneous back-ground in the wave-number domain into (5), we obtain the well known relation [2]

$$\tilde{O}(\mathbf{K} = \mathbf{k}_g + \mathbf{k}_s) = 4 \frac{\gamma_g \gamma_s}{k^2}\, \tilde{U}(k_g, k_s, k) , \tag{6}$$

where $\tilde{O}(\mathbf{K})$ is the 2D FT of the object function $O(\mathbf{r})$, $\tilde{U}(k_g, k_s)$ is the angular spectrum of the scattered field, and

$$\gamma_g = \sqrt{k^2 - k_g^2} , \quad \gamma_s = \sqrt{k^2 - k_s^2} , \tag{7}$$

$$\mathbf{k}_g = (k_g, \gamma_g) = k\hat{g} , \quad \mathbf{k}_s = (k_s, \gamma_s) = k\hat{s} . \tag{8}$$

with $\hat{g}$ and $\hat{s}$ as the unit vectors that specify the propagation directions of the decomposed plane waves to the receiver and source lines.

B. Boundary Scattering. The Born approximation is valid only for weak scattering and therefore is not applicable to large scatterers or interface reflection and scattering prob-lems. However, if the volume scatterer is large and homoge-neous, with dimensions much greater than the wavelength and has a smooth boundary, the scattering problem can be con-verted into a boundary scattering problem using a physical optics approximation [11]. Considering the case where $c(\mathbf{r})$ is constant inside the volume V, surrounded by the boundary S, we can change the volume integral (4) into a surface integral by using the second Green's theorem,

$$U(x_g, x_s) = -\int_V [\nabla^2 u(\mathbf{r}) + k^2 u(\mathbf{r})]G(x_g, \mathbf{r})\, \mathrm{d}V$$

$$= \int_S \left[u(\xi)\frac{\partial G}{\partial n} - G\frac{\partial u(\xi)}{\partial n}\right] dS , \tag{9}$$

which is a Kirchhoff integral, where ξ is a point on the surface S. Now we use the condition of smooth and weak reflecting boundary, which allows us to use the PO approximation and to neglect the multiple reflections between different parts of the boundary. Decompose $u(\xi)$ into incident field $u_0(\xi)$ and scattered field $U(\xi)$, and approximate the scattered field as

$$U(\xi) \approx u_0(\xi)R(\xi) = G(\xi, x_s)R(\xi) , \tag{10}$$

where $R(\xi)$ is the average reflection coefficient at ξ, neglect-ing the angular dependency (approximation for small incident angles). Substituting (10) into (9) we have

$$U(x_g, x_s) = \int_{S'} R(\xi)\left[G_s\frac{\partial G_g}{\partial n} - G_g\frac{\partial G_s}{\partial n}\right] d\xi , \tag{11}$$

where $G_s = G(\xi, x_s)$ and $G_g = G(x_g, \xi)$, and the integration is over S', the illuminated part of the surface. In deriving (11) we use the fact that the surface integral (9) for the incident field is zero. If the geophone is far from the surface S, then the amplitude of G_g is a slowly varying function compared with the phase change. Therefore $\partial G_g/\partial n$ is mainly from the phase change and can be approximated as

$$\frac{\partial G_g}{\partial n} = ik(\hat{r}_g \cdot \hat{n})G_g , \tag{12}$$

where $\hat{r}_g$ is the unit vector of $\mathbf{r}_g$ (the distance vector between x_g and ξ; see Fig. 1) and $(\hat{r}_g \cdot \hat{n})$ is the cosine of the span angle between $\hat{r}_g$ and $\hat{n}$. The same approximation can be obtained for $\partial G_s/\partial n$ with $(\hat{r}_s \cdot \hat{n}) = -(\hat{r}_g \cdot \hat{n}) = -\cos\theta$. Upon substitut-ing the above approximations and then taking the double Fourier transform along both the source and receiver line, (11) becomes
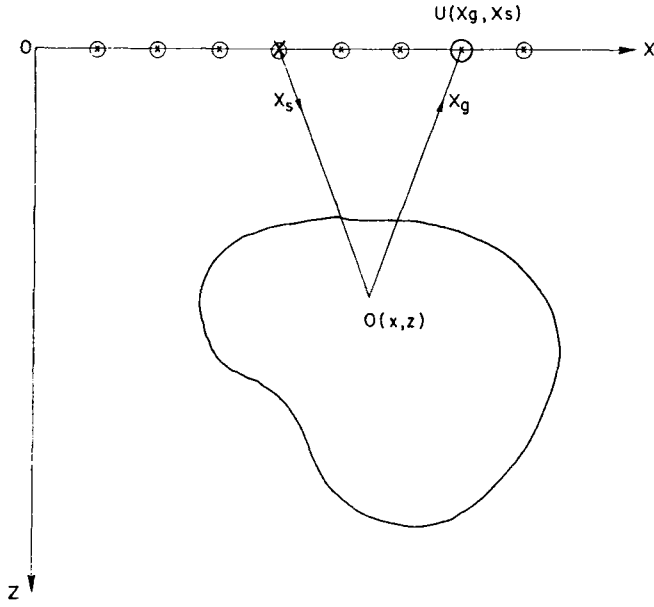
U(Xg,Xs)

O(x,z)

Figure 1. Surface reflecting profiling (SRP) geometry.

$$\tilde{U}(k_g, k_s) = \int_{S'} [2ik \cos(\theta)R(\xi)]\tilde{G}_g\tilde{G}_s \, d\xi$$

$$= \int_V [2ik \cos(\theta)R(\mathbf{r})H(\mathbf{r})]\tilde{G}_g\tilde{G}_s \, dV , \quad (13)$$

where $H(\mathbf{r})$ is the characteristic function of the surface S' defined as

$$H(r) = 1 , \quad \mathbf{r} \in S$$

$$= 0 , \quad \mathbf{r} \not\in S . \quad (14)$$

Compared with the Born approximation for volume scatterers (5), the similarity of these two expressions is evident with the substitution of $[k^2 O(\mathbf{r})]$ by $[-2ik \cos(\theta)R(\mathbf{r})H(\mathbf{r})]$. Expressing $R(\mathbf{r})H(\mathbf{r}) \cos \theta$ by $\Gamma(\mathbf{r})$ and following the same derivations as for the volume scatterers, we get

$$\tilde{\Gamma}(\mathbf{K} = \mathbf{k}_g + \mathbf{k}_s) = \frac{i2\gamma_g\gamma_s}{k} \tilde{U}(k_g, k_s, k) . \quad (15)$$

It is the same equation as for the volume scatterers (6) except for a factor $ik/2$.

Note that the PO approximation (13) is a high-frequency approximation, while the Born approximation (5) is a low-frequency approximation.

C. Spectral Coverage of MFBT. Because of the similarity between the formulas of volume scattering and boundary scattering, we will discuss in the following mainly the case of volume scattering.

From (6) we see that we can in principle reconstruct the object function if we know all the information about its spectrum from the measured data, the angular spectrum of the scattered field. Unfortunately, due to the restriction of measurement geometry for geophysical exploration, the object spectrum can be only partly recovered from the data. For the SRP geometry, the spectral coverage of SFDT with $f_0 = 50$ Hz and $c_0 = 4000$ m/s is shown in Fig. 2(a). The hatch-
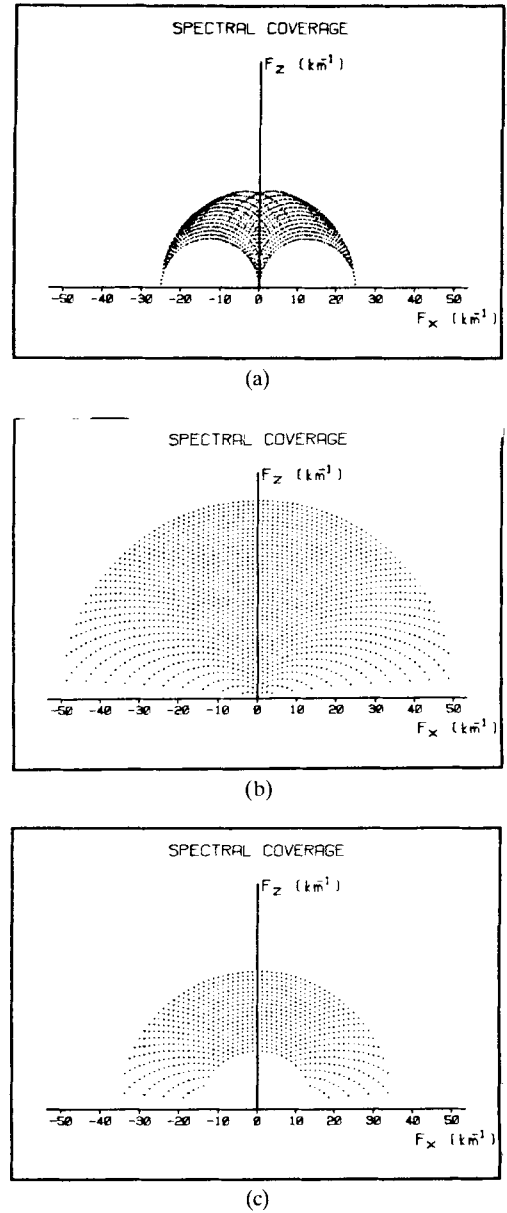

(a)

(b)

(c)

Figure 2. Spectral coverage of (a) SFDT for $f_0 = 50$ Hz, (b) MFBT for $f = 2$–100 Hz, and (c) MFBT for $f = 30$–70 Hz. Here F_x and F_z are the linear wave numbers in the x and z directions, respectively, namely, $F_x = K_x/2\pi$ and $F_z = K_z/2\pi$.

ed area in the figure represents the theoretical limit by which the spectral information of the object can be recovered by SFDT. If we neglect the absorption of the medium, then the object is a real function. Therefore, by the complex-conjugate properties of its spectrum, we can also obtain the information in the lower half-space in the spectrum domain. We see that the object spectrum is limited to the range of $2k_0$, where $k_0 = 2\pi f_0/c_0$, and there are two big holes (the blind area) in which the information is not obtainable. This is why the SFDT has poor resolution and severe image distortion. The use of a multifrequency approach can improve the performance significantly. The existing multifrequency imaging procedures are time consuming. Here we introduce a multifrequency scheme, MFBT, in which only the backscattered waves are utilized.

Combined with a special reconstruction method, MFBT becomes a very fast and efficient imaging method.

Figures 2(b) and 2(c) give the spectral coverage of multi-frequency backscattered waves [by selecting the angular spectra $\tilde{U}(k_g, k_s)$ with $k_g = k_s$] for the frequency ranges of 2–100 and 30–70 Hz, respectively (with $\Delta f = 2$ Hz). In drawing the spectral coverages, we assume 32 sources and 32 geophones with the interval of 25 m. The background velocity is assumed as 4000 m/s. We see that the coverage of MFBT is much improved over SFDT and the spectrum sampling is more uniform also. Even for a limited frequency range, such as 30–70 Hz, the spectral coverage of MFBT is still superior compared with its single-frequency counterpart.

III. RECONSTRUCTION METHODS

A. Reconstruction by Backpropagation.
Knowing the spatial spectrum of the object, we can reconstruct the object function by an inverse 2D FT:

$$O(\mathbf{r}) = \frac{1}{(2\pi)^2} \int_{-\infty}^{+\infty} \int_{-\infty}^{+\infty} d^2\mathbf{K}\, \tilde{O}(\mathbf{K}) e^{i\mathbf{K}\cdot\mathbf{r}}. \tag{16}$$

In MFBT, we choose $k_g = k_s$ for each frequency (or wave number k), and change the integration variables from (K_x, K_z) to (k_s, k). Since in this case

$$K_x = 2k_s, \quad K_z = -2\gamma_s = -2\sqrt{k^2 - k_s^2}, \tag{17}$$

we have the Jacobian

$$J(K_x, K_z | k_s, k) = \frac{\partial(K_x, K_z)}{\partial(k_s, k)} = \frac{-4k}{\gamma_s}. \tag{18}$$

Substituting (6), (17), and (18) into (16), we obtain

$$O(x, z) = \frac{1}{(2\pi)^2} \int_{-\infty}^{+\infty} \int_{-\infty}^{+\infty} dk\, dk_s \left[\tilde{U}(k_s, k) \frac{16\gamma_s}{k} e^{-i2\gamma_s z} \right] e^{i2k_s x}. \tag{19}$$

If we interpolate and stretch the data into $\tilde{U}(k_x/2, k)$ with

$$k_s = \frac{k_x}{2}, \quad \gamma_x = \sqrt{k^2 - \left(\frac{k_x}{2}\right)^2} = \gamma_s, \tag{20}$$

then

$$O(x, z) = \frac{1}{(2\pi)^2} \int_{-\infty}^{+\infty} \int_{-\infty}^{+\infty} dk\, dk_x \left[8\frac{\gamma_x}{k} \tilde{U}\left(\frac{k_x}{2}, k\right) e^{-i2\gamma_x z} \right] e^{ik_x x}. \tag{21}$$

We see that the internal integration is in a form of inverse spatial FT in the x direction. Therefore we can use the filtered backpropagation algorithm for the image reconstruction [13, 2]. First we filter the data $\tilde{U}(k_x/2, k)$ by a transfer function $8\gamma_x/k$, backpropagate to depth z using the back-propagator $e^{-i2\gamma_x z}$, and then inverse FT back to the space domain. Coherent superposition of the results from all frequencies forms the final image of MFBT. The reconstruction method of backpropagation can be easily extended to the case of vertically varying background, which will be treated in the next section.

The reconstruction of boundary image $\Gamma(x, z)$ has the same procedure as for the volume image $O(x, z)$ except for a factor of $ik/2$ multiplying the spectral data.

Let us further consider the factor $\cos\theta$ in the reconstructed image $\Gamma(\mathbf{r})$ for the case of MFBT. For a smooth surface, the scattered energy is mainly concentrated near the direction of specular reflection. Therefore, in the spectral domain, $\cos\theta$ corresponds to γ_n/k, where γ_n is the wave-number component along the surface normal $\hat{n}$. In the case of MFBT, the backscattered energy is concentrated in the directions of $\hat{n}$, i.e., $\gamma_n = k$, resulting in $\cos\theta \approx 1$ and

$$\Gamma(\mathbf{r}) \approx R(\mathbf{r})H(\mathbf{r}). \tag{22}$$

Let us compare the boundary image $\Gamma(\mathbf{r})$ and the normal gradient image of the volume scatterer under Born approximation $\partial O_B(\mathbf{r})/\partial z$, where $O_B(\mathbf{r})$ is the image reconstructed under the Born approximation. For a general reconstruction to the SRP data [2], take the normal gradient of $O_B(x, z)$,

$$\frac{\partial O_B(x, z)}{\partial z} = \frac{1}{\pi^2} \operatorname{Re} \int \int dk_s\, dk_g [-i(\gamma_s + \gamma_g)]$$
$$\times \tilde{D}(k_g, k_s)\, e^{-i(\gamma_s + \gamma_g)z}\, e^{i(k_s + k_g)x}. \tag{23}$$

The operation in the (k_s, k_g) domain is the multiplication of data by a factor $[-i(\gamma_s + \gamma_g)]$. Meanwhile, the corresponding operations for the PO approximations in the (k_s, k_g) domain is the multiplication by $[-2i\gamma_n/k^2]$. When the surface has small dip angles, or, in other words, is nearly flat, then $\gamma_n = \gamma_s = \gamma_g$, resulting in the same operation for both procedures except for a factor of k^2, which is the divergence factor of the Born approximation for high-frequency waves. We see that the PO approximation does not have the divergence problem for high frequencies.

B. Reconstruction by Direct FT.
When the background medium is homogeneous, we can change the reconstruction formula (21) into a 2D FT, similar to the case of Stolt F–K migration [10]. For a given $k_x = 2k_s$, γ is a function of k. So, doing the coordinate transform from k to γ_x using

$$\frac{dk}{d\gamma_x} = \frac{\gamma_x}{k} \tag{24}$$

and $\gamma_x = k_z/2$, (21) becomes

$$O(x, z) = \frac{1}{(2\pi)^2} \int_{-\infty}^{+\infty} \int_{-\infty}^{+\infty} dk_x\, dk_z \left(\frac{k_z}{k_i}\right)^2 \tilde{U}\left(\frac{k_x}{2}, k_i\right) e^{-ik_z z + ik_x x}, \tag{25}$$

where

$$k_i = \frac{1}{2}\sqrt{k_x^2 + k_z^2}. \tag{26}$$

The reconstruction formula (25) is a double FT, which can be implemented by the fast-Fourier-transform algorithm. The whole procedure of reconstruction can be summarized as follows:

(1) Triple-FFT the data:

$$U(x_s, x_g, t) \rightarrow \tilde{U}(k_s, k_g, \omega);$$

(2) Select the backscattered waves $\tilde{U}(k_s, k)$ for $k_s = k_g$, where $k = \omega/c_0$ with c_0 as the background velocity;

(3) Interpolate the data into $\tilde{U}(k_x/2, k)$;

(4) For each pair (k_x, k_z), find the data (with interpolation) $\tilde{U}(k_x/2, k_i)$ with $k_i = \frac{1}{2}\sqrt{k_x^2 + k_z^2}$, and weight (filter) it to obtain the object spectrum:

$$\tilde{O}(k_x, k_z) = -\frac{k_z^2}{k_i^2} \tilde{U}(k_x/2, k_i) \quad \text{for volume scattering}$$

$$= -\frac{i}{2} \frac{k_z^2}{k_i} \tilde{U}(k_x/2, k_i) \quad \text{for boundary scattering};$$

(5) 2D-inverse-FFT the object spectrum to obtain the MFBT image: $\tilde{O}(k_x, k_z) \rightarrow O(x, z)$.

Now let us compare the computation speeds of different reconstruction methods. Assume we have the same numbers of sources and receivers, i.e., $N_s = N_g$. The reconstruction method of backpropagation for MFBT will have the same order of computation speed as that for the single-frequency diffraction tomography as can be seen from (21) if $N_s \approx N_f$, where N_f is the number of frequencies used. We see that in the backpropagation method, for each k_x the computation time is mainly taken by the $N_z \times N_f$ complex multiplications. In the algorithm of direct FT, as seen from (25) for each k_x the number of complex multiplications needed is only $N_z \times \log_2 N_z$ if FFT is used. Of course, there will be an interpolation time needed for each k_x. However, when N_z and N_f are large, the time savings is remarkable. For a case of $N_f = 100$, $N_z = 128$, the factor is $N_f/(\log_2 N_z) \approx 14$. Compared to the single-frequency diffraction tomography using backpropagation for reconstruction, the speed factor of the direct FT reconstruction of MFBT is of about $N_z/(\log_2 N_z)$. Therefore, when N_z is large the MFBT will be much faster than the SFDT using backpropagation reconstruction. The reconstruction of SFDT can be also done using the interpolation FFT algorithm (see Sec. 6.4 of [15]), in which case the computation speed is roughly the same as the direct FT reconstruction of MFBT. However, due to the incomplete view-angle problem in geophysical application, usually the image quality of the interpolation-FFT reconstruction is inferior to that of the backpropagation reconstruction in the case of SFDT. For MF holography (prestack migration), the factor becomes $N_f N_z/(\log_2 N_z)$.

IV. CASE OF VERTICALLY VARYING BACKGROUND

A. Fundamental Relation under the WKBJ Approximation of the Background Green's Function.
For a vertical inhomogeneous background, the simple relation between the object spectrum and the angular spectrum of the scattered field expressed by Eq. (6) no longer holds. We turn to the more general relation (5). In this case, the Green's function in the wave-number domain under the WKBJ approximation is known as (see [14])

$$\tilde{G}(k_g, z_g; x, z; \omega) = \frac{i}{2\sqrt{\gamma_g(z_g)\gamma_g(z)}}$$

$$\times \exp\left\{i\left|\int_{z_g}^{z} \gamma_g(\zeta)\, d\zeta\right| - ik_g x\right\},$$

$$\tilde{G}(x, z; k_s, z_s; \omega) = \frac{i}{2\sqrt{\gamma_s(z_s)\gamma_s(z)}}$$

$$\times \exp\left\{i\left|\int_{z_s}^{z} \gamma_s(\zeta)\, d\zeta\right| - ik_s x\right\}, \tag{27}$$

where k_s and k_g are the wave numbers along x_s and x_g, respectively, and γ_s and γ_g are the corresponding transverse wave numbers,

$$\gamma_s(z) = \text{sgn}(\omega)\sqrt{\frac{\omega^2}{c^2(z)} - k_s^2},$$

$$\gamma_g(z) = \text{sgn}(\omega)\sqrt{\frac{\omega^2}{c^2(z)} - k_g^2}. \tag{28}$$

Substituting Eqs. (27) into Eq. (5) results in

$$\tilde{U}(k_g, z_g; k_s, z_s; \omega) = \frac{\omega^2}{4} \int\int dx\, dz$$

$$\times \frac{1}{c^2(z)\sqrt{\gamma_g(z_g)\gamma_s(z_s)\gamma_g(z)\gamma_s(z)}} O(x, z)$$

$$\times e^{-i(k_g + k_s)x} \exp\left\{i\left[\left|\int_{z_g}^{z} \gamma_g(\zeta)\, d\zeta\right| + \left|\int_{z_s}^{z} \gamma_s(\zeta)\, d\zeta\right|\right]\right\}. \tag{29}$$

The integration over x in Eq. (29) is in the form of a Fourier transform. For the surface reflection profiling geometry $z_g = z_s = 0$ and $z \geq 0$, then we have

$$\tilde{U}(k_g, k_s, \omega) = \frac{\omega^2}{4} \int dz\, \frac{\tilde{O}(k_g + k_s, z)}{c^2(z)\sqrt{\gamma_g(0)\gamma_s(0)\gamma_g(z)\gamma_s(z)}}$$

$$\times \exp\left\{i\int_0^z [\gamma_g(\zeta) + \gamma_s(\zeta)]\, d\zeta\right\}. \tag{30}$$

The integration over z on the right-hand side of Eq. (30) is not in the form of a Fourier transform, so it is impossible to obtain the simple relationship between the object spectrum and the angular spectrum of scattered wave field as in (6). We see that the angular spectrum of the scattered field measured at the surface is the superposition of those angular spectra at different depths propagating to the surface. At each depth the angular spectrum of the scattered field has a simple relation to the transverse spectrum of the object function $\tilde{O}(k_x, z)$. Equation (30) is the fundamental relation of diffraction tomography for the case of a vertically varying background for SRP measurement. However, we know that the WKBJ approximation is a smooth medium approximation which assumes that the amplitude of the wave field varies much slower than the phase term. Therefore, for layered media with strong discontinuities, the amplitude of the scattered field calculated by (30) may have large errors and require one to consider the correction using the transmission coefficient for each layer. We will not discuss this matter in detail in this article.

For MFBT only the backscattered waves are used ($k_g = k_s$). Equation (30) becomes

$$\tilde{U}(k_s, k_s, \omega) = \frac{\omega^2}{4} \int dz\, \frac{\tilde{O}(2k_s, z)}{c^2(z)\gamma_s(0)\gamma_s(z)} \exp\left\{2i\int_0^z \gamma_s(\zeta)\, d\zeta\right\}. \tag{31}$$

B. Reconstruction. Since the right-hand side of Eq. (30) is not the Fourier transform of the object function, we cannot use (16) for the reconstruction of the object function. However, from the similarity of (30) and the Fourier integral, we can derive an approximate formula of reconstruction. Let

$$k_z(z) = \gamma_g(z) + \gamma_s(z) . \tag{32}$$

We change the dummy variable z under integration on the right-hand side of Eq. (30) to z', multiply both sides of the equation by the factor

$$\frac{1}{2\pi} \frac{4}{\omega^2} c^2(z)\sqrt{\gamma_g(0)\gamma_s(0)\gamma_g(z)\gamma_s(z)} \exp\left\{ -i \int_0^z k_z(\zeta)\, d\zeta \right\} , \tag{33}$$

and integrate over k_z; then we have

$$\frac{1}{2\pi} \int dk_z\, \tilde{U}(k_g, k_s, \omega)\, \frac{4}{\omega^2}\, c^2(z)\, \sqrt{\gamma_g(0)\gamma_s(0)\gamma_g(z)\gamma_s(z)}$$

$$\times \exp\left\{ -i \int_0^z k_z(\zeta)\, d\zeta \right\}$$

$$= \frac{1}{2\pi} \int\int dz'\, dk_z \tilde{O}(k_g + k_s, z')\, \frac{c^2(z)\sqrt{\gamma_g(z)\gamma_s(z)}}{c^2(z')\sqrt{\gamma_g(z')\gamma_s(z')}}$$

$$\times \exp\left\{ i \int_0^{z'} k_z(\zeta)\, d\zeta - i \int_0^z k_z(\zeta)\, d\zeta \right\}. \tag{34}$$

We see that the right-hand side of Eq. (34) is a highly oscillating integral and only a small portion of the integrand near $z' = z$ has a significant contribution to the integral. Within this small range of $z' \approx z$, $k_z(\zeta)$ can be considered as a constant (for a vertically slowly varying medium); therefore the part of the integration over k_z on the right-hand side of Eq. (34) can be written as

$$B = \frac{1}{2\pi} \lim_{z' \to z} \int dk_z\, \frac{c^2(z)\sqrt{\gamma_g(z(\gamma_s(z)}}{c^2(z')\sqrt{\gamma_g(z')\gamma_s(z')}} \exp\left\{ i \int_z^{z'} k_z(\zeta)\, d\zeta \right\}$$

$$= \frac{1}{2\pi} \int dk_z\, \exp\{ i(z' - z)k_z \}$$

$$= \delta(z' - z) . \tag{35}$$

Substituting Eq. (35) into (34) and integrating over z' yields

$$\tilde{O}(k_g + k_s, z) = \frac{1}{2\pi} \int dk_z \tilde{U}(k_g, k_s, \omega)\, \frac{4}{\omega^2}\, c^2(z)$$

$$\times \sqrt{\gamma_g(0)\gamma_s(0)\gamma_g(z)\gamma_s(z)}$$

$$\times \exp\left\{ -i \int_0^z k_z(\zeta)\, d\zeta \right\}. \tag{36}$$

We now change the integration variable from k_z to ω. Using Eqs. (28) and (32), we have

$$\frac{dk_z}{d\omega} = \frac{\omega k_z}{c^2(z)\gamma_g(z)\gamma_s(z)} . \tag{37}$$

Then (36) can be written as

$$\tilde{O}(k_g + k_s, z) = \frac{1}{2\pi} \int d\omega\, \tilde{U}(k_g, k_s, \omega)\, \frac{4[\gamma_g(z) + \gamma_s(z)]}{\omega}$$

$$\times \sqrt{\frac{\gamma_g(0)\gamma_s(0)}{\gamma_g(z)\gamma_s(z)}} \exp\left\{ -i \int_0^z [\gamma_g(\zeta) + \gamma_s(\zeta)]\, d\zeta \right\}. \tag{38}$$

We see that in the case of a vertically varying background, the transverse spectrum of the object function at each depth is related to the multifrequency angular spectra of the scattered field through Eq. (38), which is the inversion of Eq. (30).

Taking the inverse Fourier transform with $K_x = k_g + k_s$ of Eq. (38) results in the reconstruction formula in the spatial domain,

$$O(x, z) = \frac{1}{(2\pi)^2} \int\int d\omega\, dK_x \left[\frac{4[\gamma_g(z) + \gamma_s(z)]}{\omega} \sqrt{\frac{\gamma_g(0)\gamma_s(0)}{\gamma_g(z)\gamma_s(z)}} \right.$$

$$\left. \times \tilde{U}(k_g, k_s, \omega) \exp\left\{ -i \int_0^z [\gamma_g(\zeta) + \gamma_s(\zeta)]\, d\zeta \right\} \right] e^{iK_x x} . \tag{39}$$

For MFBT, $k_g = k_s$ for each frequency (or wave number k), $k_x = 2k_s$ and $\gamma_x = \gamma_g = \gamma_s$. Therefore Eq. (39) can be written as

$$O(x, z) = \frac{1}{(2\pi)^2} \int\int d\omega\, dk_x \left[\frac{8\gamma_x(0)}{\omega} \tilde{U}\left(\frac{k_x}{2}, \omega \right) \right.$$

$$\left. \times \exp\left\{ -i2 \int_0^z \gamma_x(\zeta)\, d\zeta \right\} \right] e^{ik_x x} . \tag{40}$$

We see that the backpropagation reconstruction formula for a vertically varying background is the same as for the constant background except for a phase factor of the backpropagator.

Note that the backpropagation only performs phase corrections. This is the result of the WKBJ approximation which is valid for smoothly varying media. Actually, the interface reflection in a layered medium will reduce the amplitude of the observed scattered field. That effect has not been taken into account in our method.

For the case of constant background, Eq. (40) reduces to (21). Because the backpropagation in the MFBT is performed plane by plane, the computation time of backpropagation for vertically varying background is the same as for the constant background. However, for image reconstruction, it needs a little more computation time for a vertically varying background, because the value of γ_s must be calculated for each frequency ω as well as for each depth z.

V. NUMERICAL EXPERIMENTS

A. Volume Scattering in Constant Background. First we test the point scatterer response (spread function) of MFBT and compare with those of the single-frequency method SFDT and other more time-consuming multi-frequency methods, such as the MF holography (prestack migration).

We put a point scatterer at $x = 400$ m, $z = 300$ m. The image space is limited to 775×500 m^2 with $\Delta x = 25$ m, $\Delta z = 20$ m and a background velocity $c_0 = 4000$ m/s. The scattered

field is generated by Born approximation either in (x_s, x_g, t) domain or in (x_s, x_g, f) domain with 32 sources and 32 receivers $(N_s = N_g = 32)$. We reconstruct the images of MFBT using data with frequency ranges of 2–100, 10–90 and 30–70 Hz at intervals of $\Delta f = 2$ Hz. Figures 3(a), 3(b) and 3(c) show the spectra obtained from the data for these three frequency ranges, respectively. It is known that the theoretical spectrum of this point object should be a uniform one. Therefore, from these figures we can see how much information has been recovered from the data for each case. Due to the limited aperture of the measurement, the spectral coverages in Fig. 3 differ from the theoretical ones shown in Fig. 2 in which an infinite aperture is assumed. The effect of the finite aperture manifests itself not only in the distortion of image, but also in the reduction of the amplitude value. This effect has been addressed elsewhere [15] and will not be further discussed here. The reconstructed images by MFBT for these three frequency ranges are shown in Figs. 4(a), 4(b), and 4(c), respectively. In the figures, we show both the real part (left) and the amplitude (right) of the image field. An ideal reconstruction should recover the real object function without an imaginary part. However, due to the incomplete spectral coverage caused by the limited aperture and frequency range, the actual image becomes complex with an oscillating real part. Meanwhile the amplitude image presents the envelope of the image field and therefore gives a smoothed counterpart of the real-part image. For the SRP geometry, the horizontal resolution (the width of the point image) is much controlled by the relative aperture (the aperture-depth ratio), while the depth resolution depends basically on the frequency range. We see that the resolution and the image quality are deteriorated when the frequency range shrinks. Figures 4(d) and 4(e) give the corresponding results by SFDT $(f_0 = 50$ Hz) and by MF holography, respectively, for comparison. It is evident that the image by MFBT has a much improved resolution and image quality, together with a faster computation speed, over the single-frequency method SFDT. Also, we can see that MFBT keeps essentially the same merit of multifrequency methods as compared with MF holography or prestack migration, but with much faster computation speed.

Next we test the horizontal and vertical resolution using three point scatterers separated by one wavelength of the central frequency 50 Hz as the targets. Figure 5(a) is the result of MFBT. We can see these points are well separated in their images. In comparison, Fig. 5(b) gives the result of SFDT $(f_0 = 50$ Hz) showing its poor resolving power.

To test the resolution of MFBT for more complex objects we choose, as an example, a letter "P" composed of 12 points separated by one wavelength of the central frequency. In Figs. 6(a) and 6(b) are the results of MFBT reconstruction using the frequency ranges of 10–90 and 30–70 Hz, respectively. We see the excellent image quality for the case of broad-band frequency 10–90 Hz. However, even with the reduced frequency range of 30–70 Hz, the quality of image is still acceptable.

B. Boundary Scattering in Constant Background.

To see the difference between the volume scattering and boundary scattering reconstruction, we use a model of uniform cylinder (disk) with its center located at $x = 400$ m and $z = 300$ m. The data is generated in the (x_s, x_g, f) domain with 32 sources
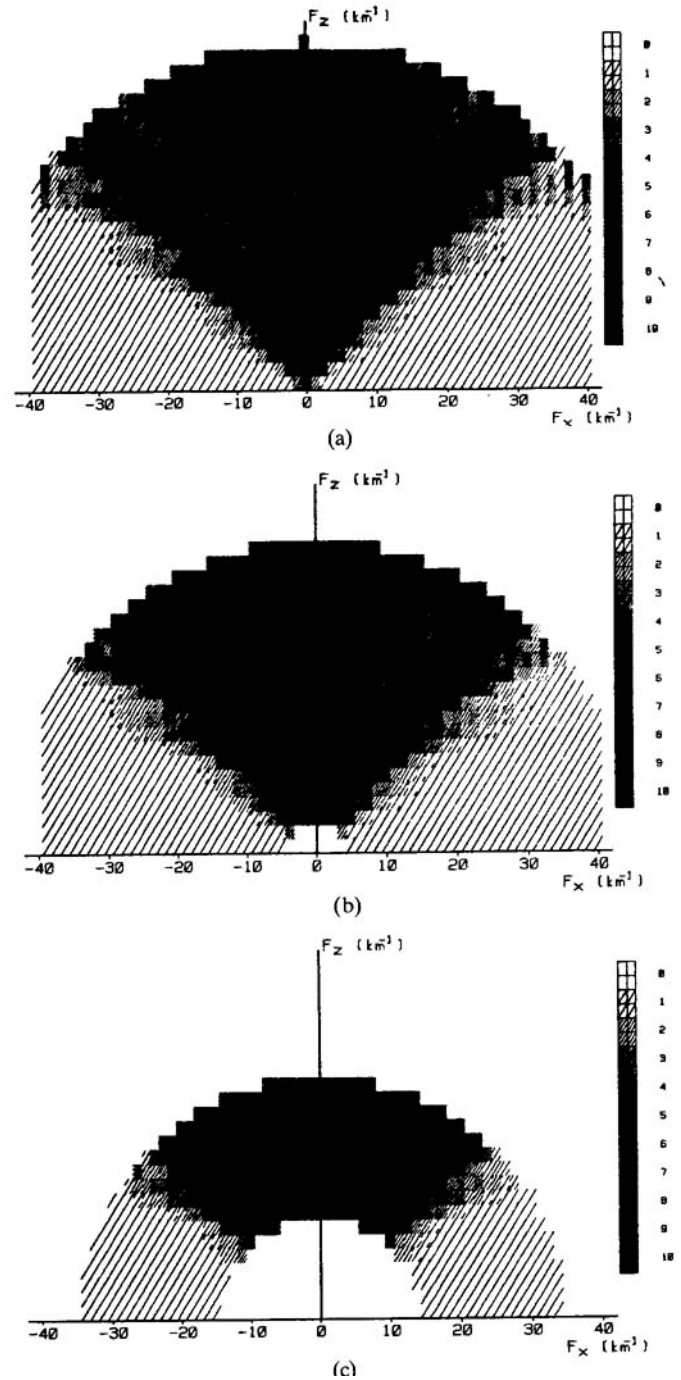

Figure 3. Object spectra derived by MFBT of a point scatterer for (a) $f = 2 - 100$ Hz, (b) $f = 10$–90 Hz, and (c) $f = 30$–70 Hz. For the definition of F_x and F_z, see Fig. 2.

and 32 receivers. The image space is 800×800 m^2 with $\Delta x = \Delta z = 25$ m, the background velocity is $c_0 = 4000$ m/s, and the disk's velocity is $c_p = 4400$ m/s. The MFBT data was generated using the Born approximation

$$U(x_g, x_s, k) \approx \sum_{j=1}^{N} O_j(x, z) \, \Delta s_j G_s(r_j, x_s) G_g(x_g, r_j)$$

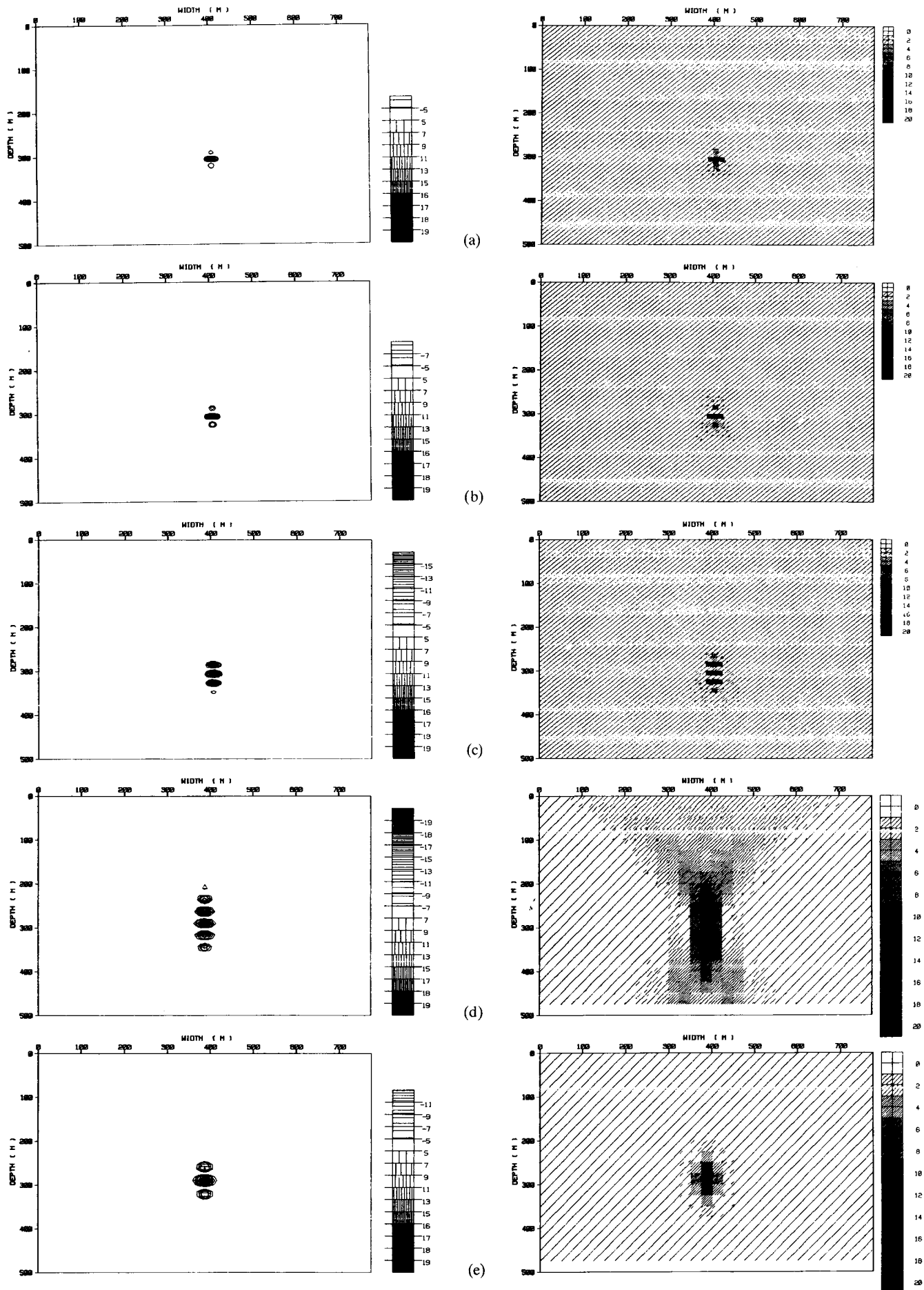$$= -i \frac{k}{8\pi} \sum_{j=1}^{N} O_j \frac{\Delta s_j}{\sqrt{R_s R_g}} \exp\{ik(R_s + R_g)\}, \quad (41)$$

Figure 4. Reconstructed images of a point scatterer by (a) MFBT for $f = 2$–100 Hz, (b) MFBT for $f = 10$–90 Hz, (c) MFBT for $f = 30$–70 Hz, (d) SFDT for $f_0 = 50$ Hz, and (e) prestack migration for $f = 30$–70 Hz. In the figures, the real parts and the amplitudes of the image fields are shown on the left and right, respectively. The real-part image has high resolution but is oscillating, while the amplitude image is a smoothed counterpart of the real-part image with lower resolution. For details see the text.
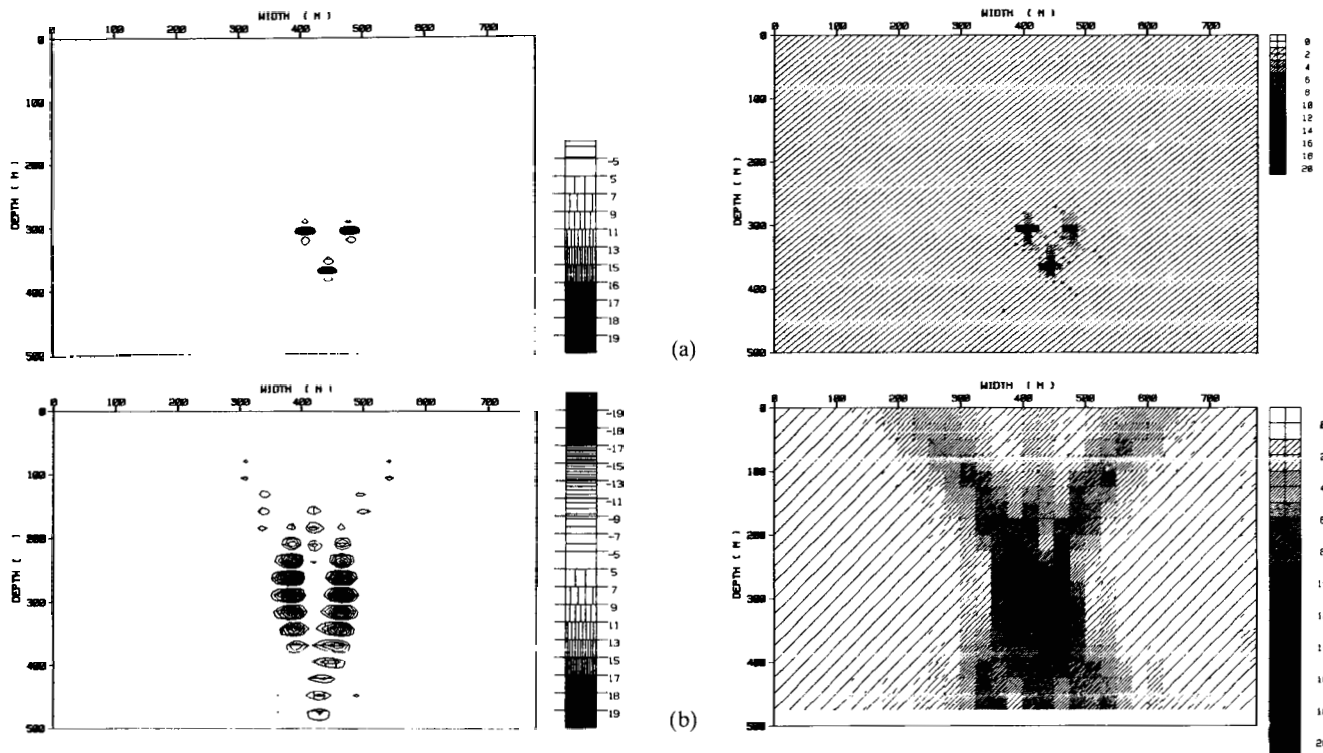
Figure 5. Reconstructed image of three point scatterers by (a) MFBT for $f = 2-100$ Hz, and (b) SFDT for $f_0 = 50$ Hz. On the left are real-part images and on the right, amplitude images. See captions of Fig. 4.
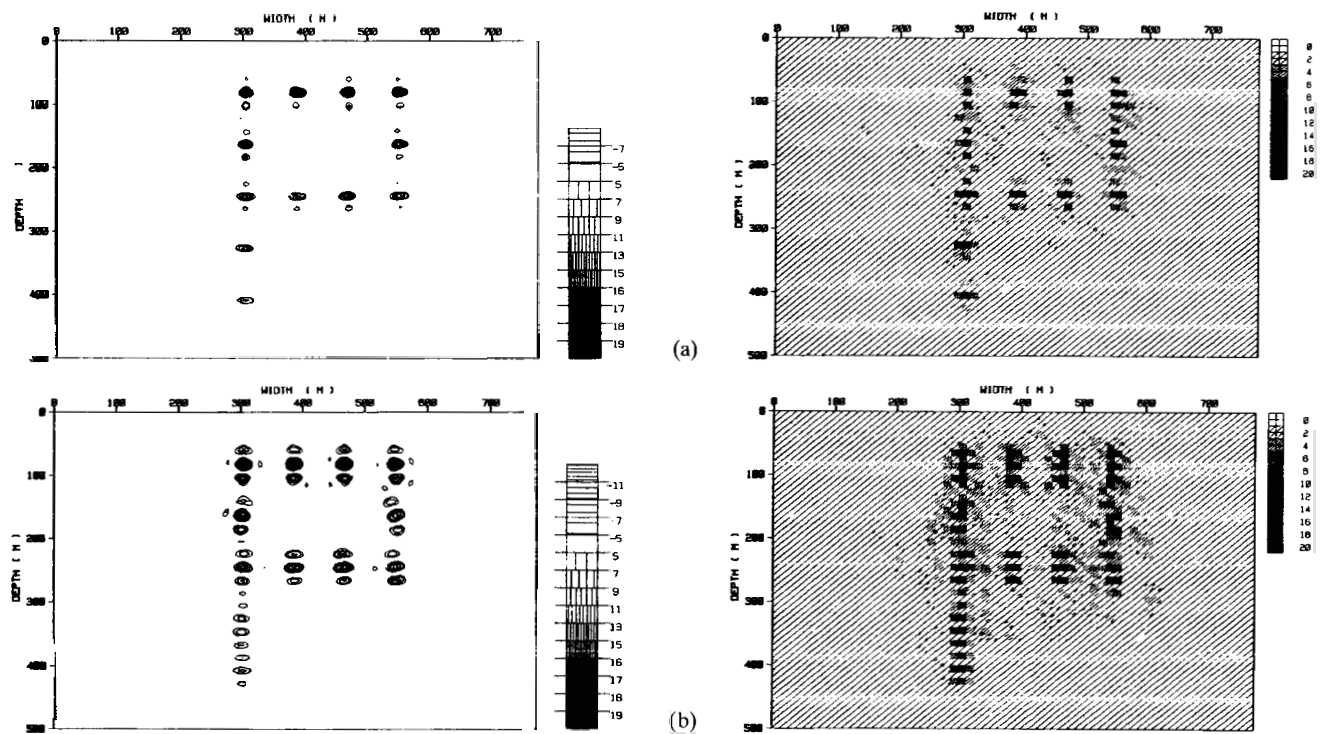
Figure 6. Reconstructed image of a letter "P" by (a) MFBT for $f = 10-90$ Hz, and (b) MFBT for $f = 30-70$ Hz. On the left are real-part images and on the right, amplitude images. See caption of Fig. 4.
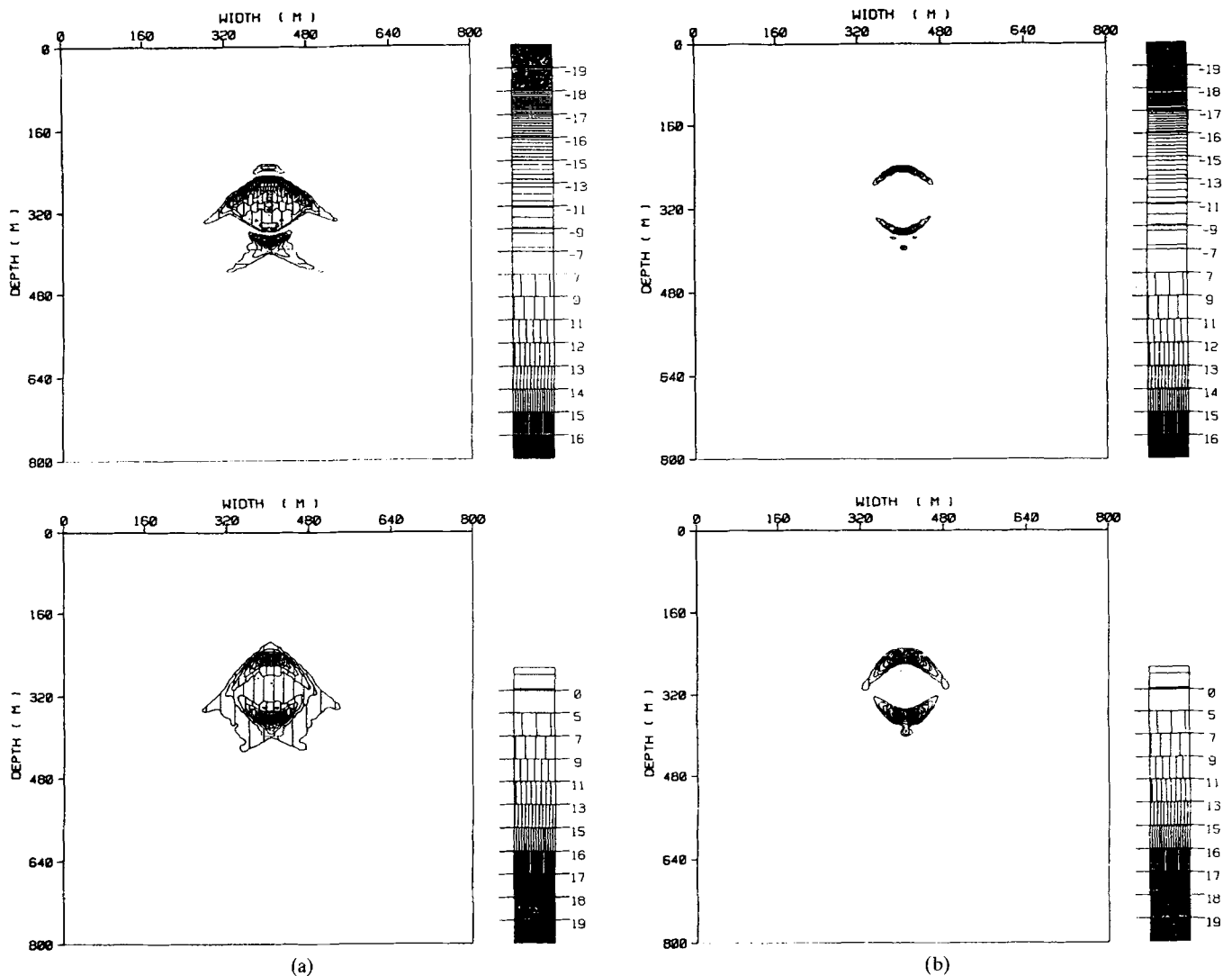
Figure 7. Reconstructed images using MFBT for $f = 2$–100 Hz for (a) volume scattering and (b) boundary scattering. On the left are real-part images and on the right, amplitude images. See caption of Fig. 4. The model is a disk of 120 m $(3\lambda_{min})$ in diameter.

where $O_j(x, z)$ is the object value at each cell $r_j = (x_j, z_j)$ and Δs_j is the area of the jth cell. When the central point of a cell falls out of the limit of the boundary of the disk, the area is neglected. The disk has a diameter of $3\lambda_{min}$ and was sampled with $\Delta x = \Delta z = 0.1 \lambda_{min}$. Figures 7(a) and 7(b) show the reconstructions using MFBT for volume scattering and for boundary scattering, respectively. As before, the right-hand sides are the amplitude images and the left-hand sides are the real-part images. We see that the boundary reconstruction algorithm has a better image of the outline of the disk.

C. Vertically Varying Background

1. Calculation of the Synthetic Data. The simplest and fastest method of calculating the synthetic scattered field is to use Eq. (31) and generate the data directly in the wave-number domain. However, this type of data cannot simulate the effect of finite aperture. The other options are finite difference or ray-Born algorithms. Because a large number of sources (in our case, 32 sources) is used in the simulations, the procedure of generating synthetic data would be very time

consuming by the above-mentioned two methods. Here we adopt a WKBJ-Born algorithm for this special purpose. Given the object function $O(x, z)$, its spectrum can be calculated by FT and then the scattered field in the wave-number domain can be generated using (29). The inverse FT of the wave-number domain data can serve as the spatial domain data. However, in order to reduce the Gibbs phenomena caused by the high-wave-number cut in spectral domain we resample $O(x, z)$ with a much smaller Δx and therefore obtain $\tilde{U}(k_g, k_s, \omega)$ with much higher k_g and k_s. This resampling technique has been proved to be effective. We test this technique by comparing the data with the data generated by the formula of Born scattering in the space domain [Eq. (41)] for a point scatterer in a homogeneous medium. Figure 8 shows the comparison of reconstructed images using different types of synthetic data. The geometry of measurements is the same as for Fig. 4 (with the exception of $\Delta z = 10$ m). In Fig. 8 the cross sections along the vertical and horizontal directions passing through the scattering point are shown on the left and right, respectively, for (a) the original object, (b) the recon-
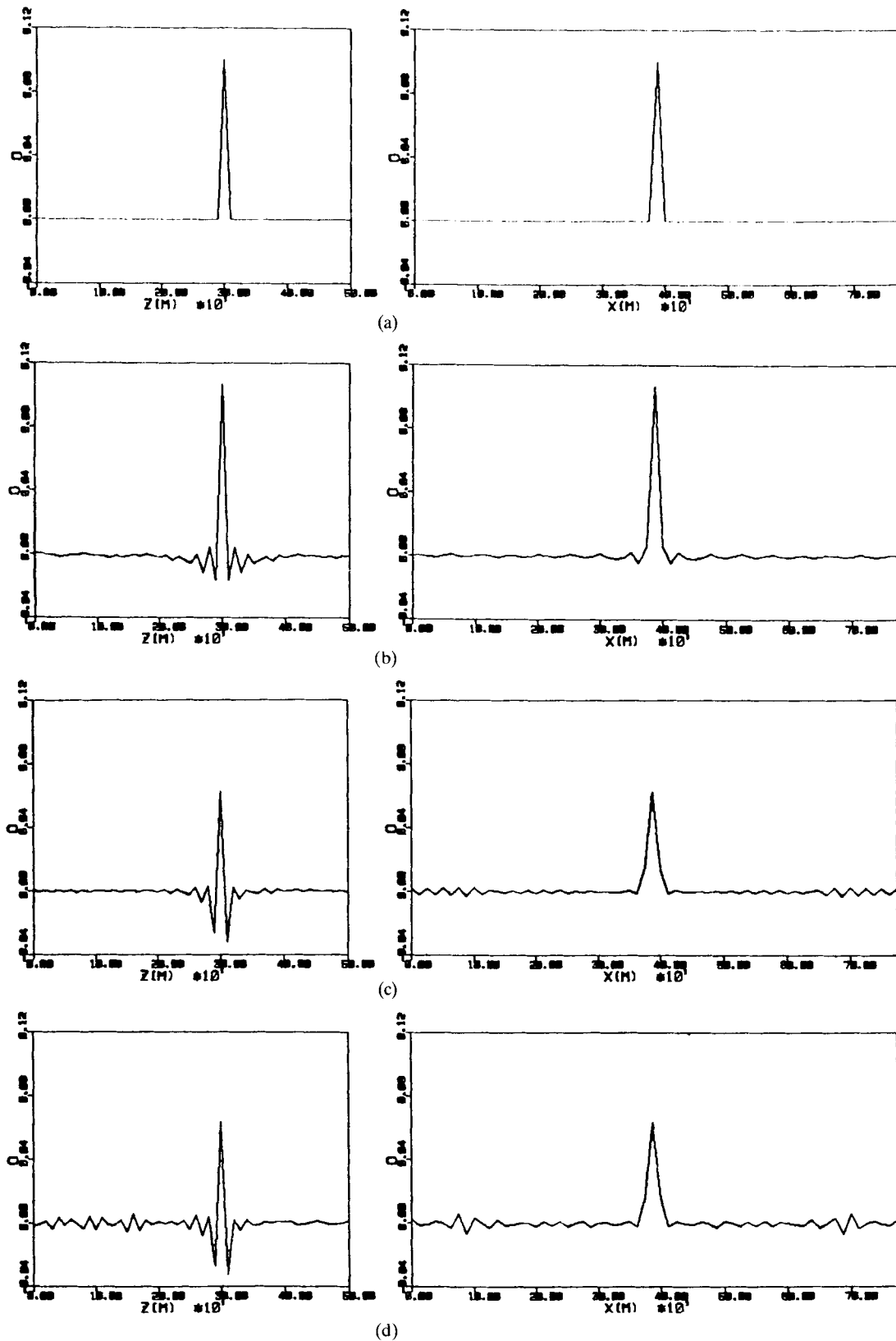
Figure 8. A comparison of the images of the MFBT obtained by using three different kinds of the scattered data in a homogeneous background ($c_0 = 3000$ m/s). The curves are the cross sections of the real parts of the object functions in vertical (left) and horizontal (right) directions through the position of the point scatterer. (a) The original object function, (b) reconstructed results from the data in wave-number domain, (c) reconstructed results from the data in spatial domain, (d) reconstructed results from the data in spatial domain generated by resampling and transforming using FFT.
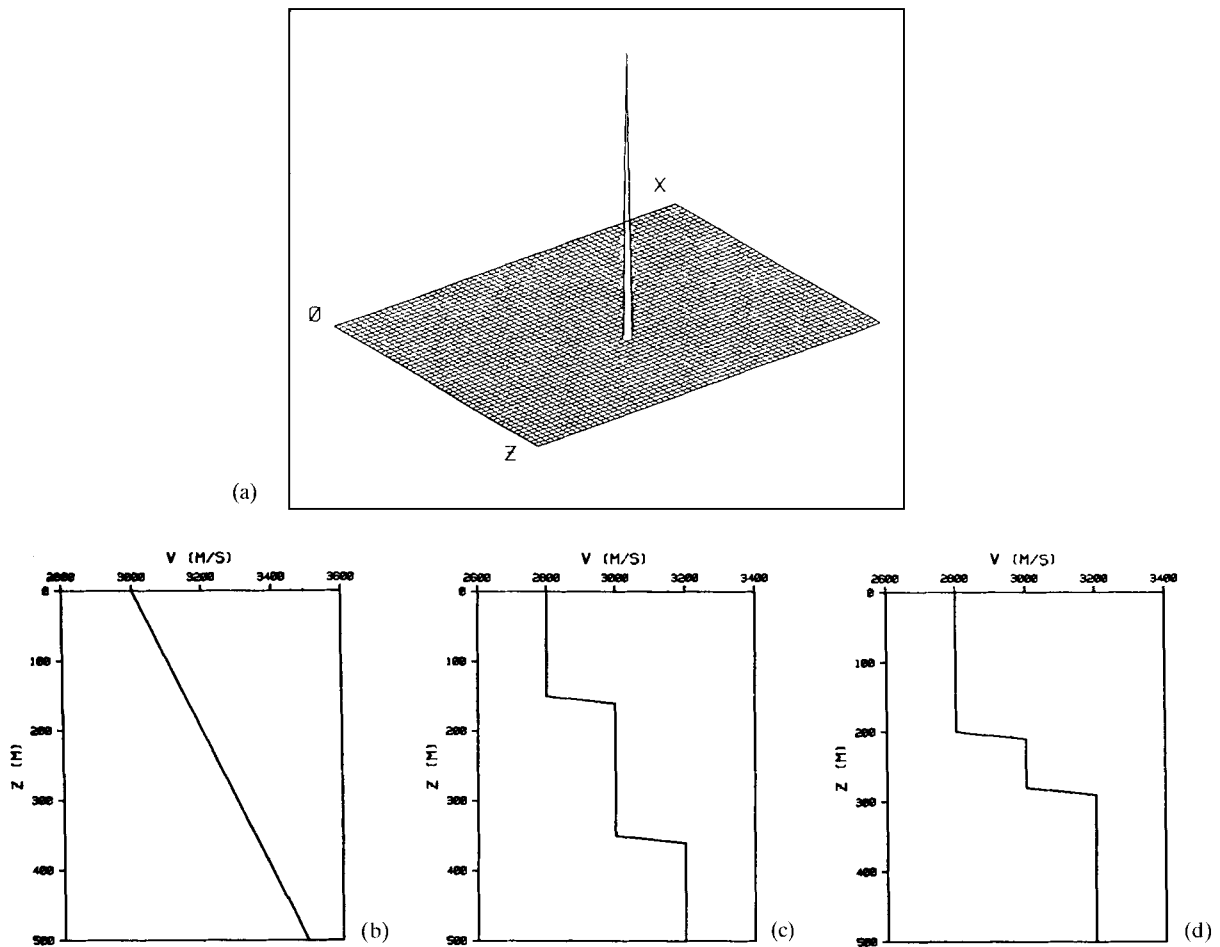
Figure 9. The model of the point scatterer and the velocities of the backgrounds. (a) The point scatterer, (b) the velocity of the linear background, (c) the velocity of the layered background 1, and (d) the velocity of the layered background 2.
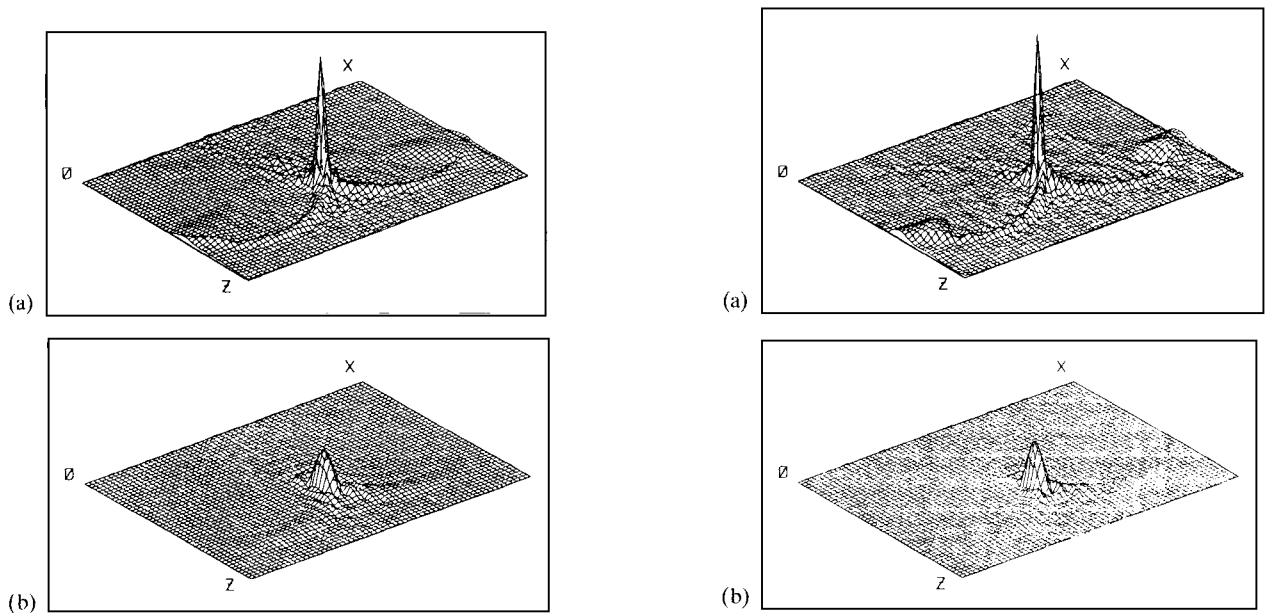
Figure 10. The reconstructed images (amplitudes of the object function) of the point scatterer by the MFBT in the linear background for (a) $f = 10-90$ Hz and (b) $f = 10-50$ Hz.
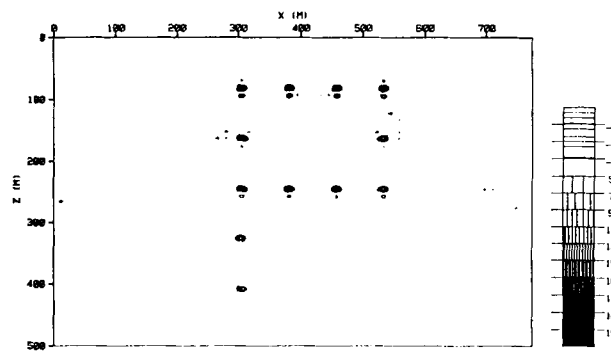

Figure 11. The reconstructed images (amplitudes of the object function) of the point scatterer by the MFBT in the layered background for (a) $f = 10-90$ Hz and (b) $f = 10-50$ Hz.
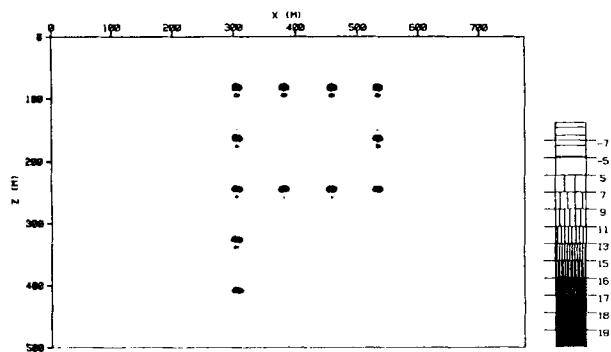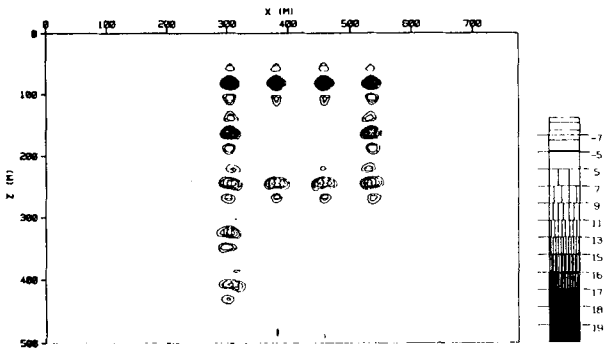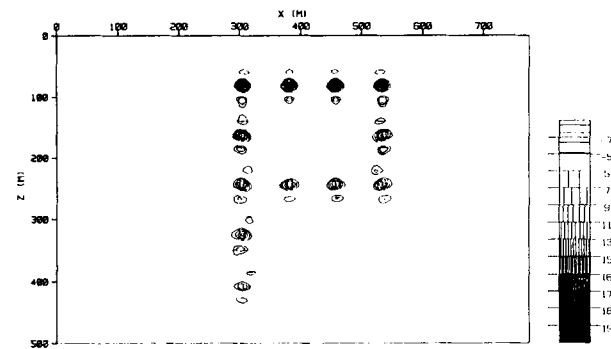
Figure 12. The reconstructed images (real parts) of the letter 'P" by the MFBT in the linear background for (a) $f = 10-90$ Hz and (b) $f = 10-50$ Hz.
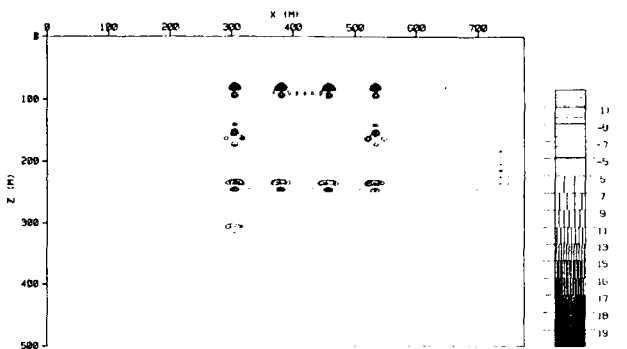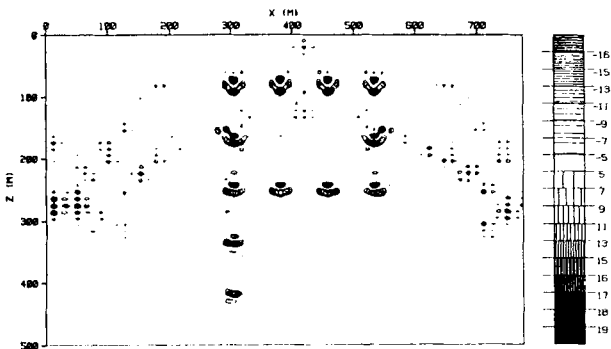
Figure 13. The reconstructed images (real parts) of the letter "P" by the MFBT in a layered background. (a) Reconstructed image for $f = 10-90$ Hz and (b) reconstructed image for $f = 10-50$ Hz.

Figure 14. The reconstructed images (real parts) by the MFBT in homogeneous background using the spatial domain data for the linear background. The velocity of the homogeneous background is (a) $c_0 = 3000$ m/s, (b) $c_0 = 3250$ m/s, and (c) $c_0 = 3500$ m/s. Frequency band: 10-90 Hz; $\Delta f = 2$ Hz.

structed image using data generated in the wave-number domain by (29), (c) image using data generated in the space domain by Born approximation (41), and (d) image using data generated in the space domain by a resampling FFT technique (with a resampling rate of 4). We see that the strong oscillations of curves in (c) and (d) are caused by the effect of finite aperture. The oscillation of curve (b) along the z direction is from the effect of the limited frequency band. We also see that the image from the data generated by the resampling FFT algorithm is about the same as that by direct calculation in the space domain using the Born approximation which is much more time consuming. In the following we will use the resampling FFT algorithm for the numerical simulation in vertically varying background.

2. Examples of Image Reconstruction. The model of the point scatterer is shown in Fig. 9(a) and the backgrounds used are the linear background with a velocity gradient of 1 km/s/km in Fig. 9(b), and the layered backgrounds 1 and 2 in Figs. 9(c) and 9(d), respectively. The images of Figs. 10(a) and 10(b) are for the cases of linear background with $f = 10 - 90$ Hz and $f = 10-50$ Hz ($\Delta f = 2$ Hz), respectively. We see that both the amplitude and the resolution of the image are reduced substantially by the decrease of the frequency range. Figures 11(a) and 11(b) give the results of reconstruction for the case of the layered background 1 where the point scatterer is located in the second layer. We see that the image quality is about the same as for the case of linear background.

To test the performance of the MFBT for more complex objects in the case of a vertically varying background, we choose again the letter "P" as the object. For the linear velocity background as shown in Fig. 9(b), the reconstructed images of letter "P" by the MFBT are displayed in Figs. 12(a) and 12(b) for $f = 10 - 90$ Hz and $f = 10-50$ Hz, respectively. Next, we put the same object in the layered background 2. The reconstructed image by MFBT with $f = 10-90$ Hz and $f = 10-50$ Hz are given in Figs. 13(a) and 13(b), respectively. We can see the good quality of reconstruction for all the cases. In addition, we see also from these figures that the deeper the scatterer is from the receiver line, the smaller is the amplitude of its reconstructed image. This again is the effect of limited aperture.

For scattered wave fields in a variable background, the image quality will be greatly deteriorated if one uses a reconstruction method of constant background for imaging. To demonstrate this, we use the scattered field data of the letter "P" in the linear background given in Fig. 9(b) and reconstruct the image using the MFBT in constant background. We choose the velocity of the background as 3000, 3250, and 3500 m/s, successively, and give the reconstructed images (real-part images with $f = 10-90$ Hz) in Figs. 14(a), 14(b), and 14(c), respectively. Compared with the corresponding results of Fig. 12(a), the oscillation and distortion of all three images are very serious. The image quality of Fig. 14(b) is slightly better than the other two because 3250 m/s is the average velocity of the linear background.

VI. CONCLUSIONS

(1) The use of a multifrequency approach in diffraction tomography can increase the information coverage of the object spectrum and partly fill the "blind areas" in the

spectral domain of single-frequency reconstruction, and therefore improve the resolution and the image quality.

(2) We derive both the formulas of MFBT (multifrequency backscattering tomography) for volume scattering use the Born approximation and that for boundary scattering using the physical optics approximation. The latter is applicable for the case of large homogeneous volume scatterer or strong interface reflection and scattering. It is shown that under certain approximations the boundary scattering problem ends up with the same formulas except for a factor which modifies the object spectrum. Compared with the reconstruction of normal derivatives using Born approximation, the boundary scattering formulation does not have the problem of high-frequency divergence.

(3) We extend the formulation from constant background to vertically varying background using WKBJ approximation for the background Green's function. It is shown that under certain approximation the backpropagation method of reconstruction becomes the same as the case of constant background except for a phase factor of the backpropagator. It is also shown through numerical simulations that the image quality would be greatly deteriorated if the reconstruction method of constant background was adopted for the case of the vertically varying background.

(4) The fast direct FT reconstruction algorithm is preferable for the case of constant background, while the backpropagation method may be used for both the cases of constant and vertically varying backgrounds.

(5) Multifrequency backscattering tomography is a fast algorithm, especially with the direct FT reconstruction method for constant background, even faster than the single-frequency method by a factor of about $N_z/\log_2 N_z$. The method also keeps almost the same quality of image as the other multifrequency methods, as can be seen from the comparison by numerical simulations. Therefore the method is suitable for 3D image reconstruction. The image obtained can serve as an initial model for a more sophisticated non-linear inversion. Although the formulation and numerical examples in this article are given for the 2D case, the theory and method can be extended to the 3D case in a straight-forward way.

REFERENCES

1. A. J. Devaney, "Geophysical diffraction tomography," *IEEE Trans.* Geosci. Electron. **GE-22**, 3-13 (1984).
2. R. S. Wu and M. N. Toksöz, "Diffraction tomography and

multi-source holography applied to seismic imaging," *Geophysics* **52**, 11–25 (1987).

3. T. W. Lo, M. N. Toksöz, S. H. Xu and R. S. Wu, "Ultrasonic laboratory tests of geophysical tomographic reconstruction," *Geophysics* **53**, 947–956 (1988).

4. R. G. Pratt and M. H. Worthington, "The application of diffraction tomography to cross-hole seismic data," *Geophysics* **53**, 1284–1294 (1988).

5. A. Tura, L. R. Johnson, E. L. Majer and J. E. Peterson, "Application of diffraction tomography to fracture detection," *Geophysics* **57**, 245–257 (1992).

6. T. W. Lo and G. W. Purnell, "Imaging salt pods with Born inversion," *Expanded Abstracts of the 60 Annual International Meeting of the SEG*, **2**, 1215–1218 (1990).

7. W. C. King, A. J. Witten and G. D. Reed, "Detection and imaging of buried wastes using seismic wave propagation," *J. Environ. Eng.* **115**, 527–548 (1989).

8. A. Witten, D. D. Gillette, J. Sypniewski and W. C. King, "Geophysical diffraction tomography at a dinosaur site," *Geophysics* **57**, 187–195 (1992).

9. R. S. Wu, Y. L. Wu, C. R. Liu, C. Y. Peng and M. J. Wang, "Multi-frequency synthetic detecting holography," *Acta Geophys. Sin.* **20**, 33–38 (1977).

10. R. H. Stolt and A. K. Benson, *Seismic Migration, Theory and Practice* (Geophysical Press, London, 1986).

11. K. J. Langenberg, "Applied inverse problems for acoustic, electromagnetic and elastic wave scattering," in *Basic Methods of Tomography and Inverse Problems*, edited by P. C. Sabatier (Adam–Hilger, Bristol, 1987).

12. R. S. Wu, "Multi-frequency backscattering tomography. A fast imaging algorithm for 3D heterogeneities," *Int. Union Geod. Geophys., XX Gen Assemb.*, Vienna, August, 1991.

13. A. J. Devaney, "A filtered back propagation algorithm for diffraction tomography,' *Ultrasonic Imaging* **4**, 336–350 (1982).

14. R. W. Clayton and R. H. Stolt, 'A Born-WKBJ inversion method for acoustic reflection data," *Geophysics* **46**, 1559–1567 (1981).

15. A. C. Kak and M. Slaney, *Principle of Computerized Tomographic Imaging* (IEEE Press, New York, 1988).